






# Wideband Multimode Leaky-Wave Feed for Scanning Lens-Phased Array at Submillimeter Wavelengths

Maria Alonso-delPino , *Senior Member, IEEE*, Sjoerd Bosma , *Student Member, IEEE*,  
Cecile Jung-Kubiak , *Senior Member, IEEE*, Goutam Chattopadhyay , *Fellow, IEEE*,  
and Nuria Llombart , *Fellow, IEEE*

**Abstract**—In this article, we propose a hybrid electromechanical scanning lens antenna array architecture suitable for the steering of highly directive beams at submillimeter wavelengths with field-of-views (FoV) of  $\pm 25^\circ$ . The concept relies on combining electronic phase shifting of a sparse array with a mechanical translation of a lens array. The use of a sparse-phased array significantly simplifies the RF front-end (number of active components, routing, thermal problems), while the translation of a lens array steers the element patterns to angles off-broadside, reducing the impact of grating lobes over a wide FoV. The mechanical translation required for the lens array is also significantly reduced compared to a single large lens, leading to faster and low-power mechanical implementation. In order to achieve wide bandwidth and large steering angles, a novel leaky wave lens feed concept is also implemented. A 550-GHz prototype was fabricated and measured demonstrating the scanning capabilities of the embedded element pattern and the radiation performance of the leaky wave fed antenna.

**Index Terms**—Beam-scanning, leaky-wave feed, lens antenna array, lens-phased array, submillimeter-wave.

## I. INTRODUCTION

ARRAY technology is currently being developed at submillimeter wavelengths to enable a broad spectrum of applications including astrophysical observations, communications, radar, security screening, and spectroscopy [1]–[4]. Most of these applications require highly directive beams that can be scanned over a certain field of view with wide bandwidth. Until now, the only realistic scanning antenna architecture for submillimeter wavelengths has been the use of quasi-optical

systems combined with bulky mechanical scanners [4]–[6]. In order to achieve more compact systems, it is necessary to develop integrated beam steering antenna architectures. The challenge in developing such architectures is the need for large steering angles ( $\pm 25^\circ$ ) with large apertures (i.e., directivities larger than 40 dBi) and wide frequency bandwidths (larger than 10%).

Numerous approaches to beam steering can be found in the literature [4]–[23]. Phased arrays are the traditional architecture at microwaves, whose elements are typically placed at half-wavelength distance from each other in order to avoid the generation of grating lobes. Recently, small phased arrays have been demonstrated in integrated-circuit technology up to 530 GHz with gains up to 12 dB [7]–[9]. This approach faces a major bottleneck to reach larger gains at higher frequencies: array architectures suffer from physical constraints with packaging, either the local oscillator (LO) multiplication chain's size is larger than the radio frequency (RF) wavelength [10], [11], or it suffers high losses in the LO distribution network [11]. Another approach consists of increasing the spacing between elements, resulting in sparse phased arrays. These arrays allow scanning over limited angular ranges, as long as the grating lobes are properly attenuated by the element pattern [12]. This has been shown in the microwave regime by using leaky-wave (LW) feeds [13], [14] and subarray techniques [15], [16]. However, both the bandwidth ( $< 5\%$ ) and the beam steering angles ( $< 5^\circ$ ) are small or they suffer from high distribution network losses.

At microwave frequencies, the use of phased lens arrays with large spacing has been proposed for astrophysical applications [17]. Small lenses phased arrays with limited scanning ranges have also been developed in microwaves [18]–[20]. Specifically, it was anticipated in [20] that, in order to extend the otherwise very limited scanning capabilities, one would need to mechanically or electronically maneuver feed elements. More recently, the communications industry has also started to move in that direction; more patents are being published utilizing array of lenses with specific applications for communications in the Ka band [21]–[24].

With the support of the European Union under the ERC starting under Grant LAATHz-CC (639749) granted in 2015, we proposed the use of coherent lens arrays integrated with LW antennas and mechanical piezoelectric motors to solve the array integration problem at submillimeter wavelengths [25]. This dynamic beam steering architecture combines low mechanical complexity (reduced mass with respect to translating a single

Manuscript received July 6, 2020; revised October 1, 2020; accepted October 27, 2020. Date of publication November 16, 2020; date of current version March 3, 2021. This work was supported by the ERC Starting Grant LAA-THz-CC (639749). (Corresponding author: Maria Alonso-delPino.)

Maria Alonso-delPino was with the Jet Propulsion Laboratory, California Institute of Technology, Pasadena, CA 91109 USA, and is currently with Terahertz Sensing Group at the Technical University of Delft, 2628 CD Delft, The Netherlands (e-mail: m.alonsodelpino@tudelft.nl).

Sjoerd Bosma and Nuria Llombart are with the Terahertz Sensing Group, Technical University of Delft, 2628 CD Delft, The Netherlands (e-mail: s.bosma@tudelft.nl; n.llombartjuan@tudelft.nl).

Cecile Jung-Kubiak is with the Advanced Optical and Electromechanical Microsystem Group, California Institute of Technology, Pasadena, CA 91109 USA (e-mail: d.jung@jpl.nasa.gov).

Goutam Chattopadhyay is with the Submillimeter-Wave Advanced Technology Group, Jet Propulsion Laboratory, California Institute of Technology, Pasadena, CA 91109 USA (e-mail: goutam.chattopadhyay@jpl.nasa.gov).

Color versions of one or more figures in this article are available at <https://doi.org/10.1109/TTHZ.2020.3038033>.

Digital Object Identifier 10.1109/TTHZ.2020.3038033

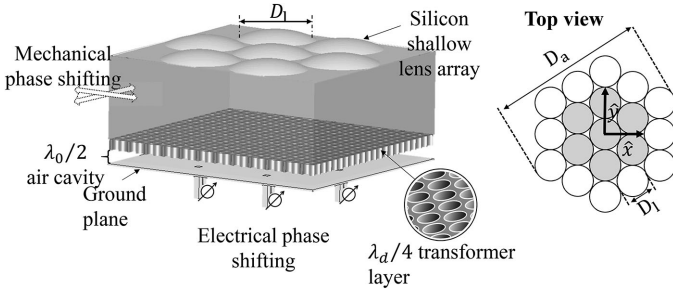


Fig. 1. Geometry of the proposed scanning lens-phased array that uses a combination of mechanical phase shifting of a silicon lens array and electronic phase shifting in the feeds. The lens array is fed by a multi-mode LW feed that uses a synthesized quarter-wavelength transformer on top of a resonant air cavity. The inset shows the lens array layout with a circular aperture of  $D_a$  and 19 lenses of diameter  $D_l$ . The prototype array consists of seven elements (shaded).

lens) with a greatly reduced number of phase shifters. The geometry of the proposed array based on a LW feed is shown in Fig. 1. The array is composed of a sparse array of active RF array elements distributed over the whole array aperture coupled to a layer of actuated lenses (one per array element). The single layer of lenses can be translated mechanically relative to the ground plane, using an implementation similar to [26], to achieve element pattern scanning, while the active RF phase shifters cause array factor (AF) scanning. The grating lobes resulting from the array's sparsity are attenuated by the directive element patterns of the lenses.

In this article, we demonstrate a new LW feed that increases the bandwidth and the array's steering performance with respect to previous LW implementations [27]. The proposed feed uses a quarter wavelength layer of a certain permittivity, added in-between the lens and the air cavity, to generate multiple leaky modes in this cavity, which helps to enhance the aperture efficiency, similar to what was proposed in [28] for illuminating reflectors. Additionally, this dielectric layer ensures impedance matching of the feed without a double-slot iris typically used in such LW antennas, which significantly simplifies the fabrication process. Simulated results of the lens antenna array show aperture efficiencies greater than 80% for a bandwidth of 35%. Scanning angles of  $\pm 20^\circ$  can be achieved with a scan loss lower than 2 dB. We have fabricated a prototype at 550 GHz and measured the steerable element array embedded pattern, showing good agreement with the simulations, and thus validating the concept.

The article is structured as follows. Section II defines the phased lens array design guidelines, while Section III explains the novel multimode LW waveguide feed and its performance. Next, Section IV describes the lens antenna and lens-phased array performances. Section V details the prototype manufacturing and Section VI corroborates the presented simulations with measurements. Conclusions are drawn in Section VII.

## II. SCANNING LENS-PHASED ARRAY DESIGN GUIDELINES

In this section, we describe the main design guidelines for the lens feed that impact the performance of the proposed scanning

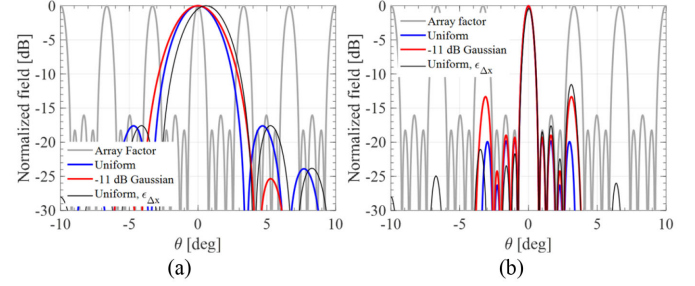


Fig. 2. (a) Broadside array factor and element patterns of the 19-element hexagonal array shown in the inset of Fig. 1 with  $D_l = 20\lambda_0$  and uniform amplitude (blue) or  $-11$  dB Gaussian taper (red) apertures. The impact of the mechanical tolerance  $\epsilon_{\Delta x} = 58 \mu\text{m}$  and  $N_{RF} = 5$  is shown in black for a uniform aperture; (b) Array pattern for the same cases as in (a).

lens-phased array architecture. To describe these guidelines, we consider a circular array aperture of diameter  $D_a = 100\lambda_0$ , which can theoretically provide up to 50 dBi of directivity, a number that is in line with future needs of security [4] and space planetary applications with Cubesat/SmallSat [29]. The considered array is filled with a hexagonal arrangement of 19 circular lenses with diameter  $D_l = 20\lambda_0$ , as shown in the inset of Fig. 1, which is a reasonable dimension for the aforementioned applications.

### A. Electronic Phase Shifting: Array Factor

A phase shift is applied to each array element, which leads to an array factor (AF) that is associated with the periodicity of the array and with this, the beam can be steered electronically. The number of active elements is reduced by a factor  $\sim (2D_l/\lambda_0)^2$  compared to a fully sampled array. It is well known that if the periodicity of the array is larger than  $\lambda_0/2$ , grating lobes can appear at angles  $\theta_g^n$ . For example, in the considered geometry, grating lobes will appear at multiples of  $\theta_g = 3.3^\circ$ , as shown in Fig. 2(a). The electronic phase shift enables the steering of the array factor (AF). Since the AF has multiple beams due to the grating lobes, it is only necessary to scan the AF in the angular region from broadside until the first grating lobe  $\theta_g^1$ . This is because the mechanical translation of the lens allows the array to scan to larger angles than  $\theta_g^1$  by steering the element pattern toward the different grating lobes  $\theta_g^n$ . The overall phase shift required to scan the main beam of the array to angle  $\theta_s$  is given by  $\psi_s(\theta_g) = 2\pi N_{RF}$  with  $N_{RF} = D_a/D_l$ . This implies a reduction of the overall phase shift by a factor of  $\sin(\theta_s) D_l/\lambda_0 = 10$ . In our example with  $N_{RF} = 5$ , a phase shift of  $10\pi$  is sufficient to scan any angle. By contrast, a fully sampled circular array of  $D_a = 100\lambda_0$  scanned toward  $30^\circ$  will require a phase shifting of  $2\pi D_a \sin 30^\circ/\lambda_0 = 100\pi$ .

In Fig. 2(a), the element radiation pattern from a uniform circular aperture of diameter  $D_l = 20\lambda_0$  is superimposed on the 19 elements hexagonal array factor. It is evident that the highest resulting grating lobe of the combined pattern is around  $-19$  dB, see Fig. 2(b). The level of this first grating lobe is related to the width of the main beam of the element pattern. Therefore, this level will be the lowest when the array element has a uniform

aperture illumination. A comparison of the patterns resulting from an array illuminated with uniform circular apertures and with Gaussian apertures of  $-11$  dB edge taper is shown in Fig. 2(a) and 2(b). For this second case, the main beam of the element pattern is wider and the grating lobes of the combined pattern increase to  $-12$  dB, which may still be acceptable for many applications. For instance, the use of synthetic apertures via interferometry leads to grating lobe levels of  $-6.6$  dB [30]. However, what is evident from this figure is that the grating lobe level of the array pattern improves with the aperture efficiency of the array elements. Therefore, lens feeds with top hat patterns are needed to achieve low grating lobe levels.

### B. Mechanical Phase Shifting: Element Pattern

The number of lens element pattern beams that are steered in a certain FoV with a mechanical translation of a lens can be approximated as

$$N_l = \frac{\text{FoV}}{\Delta\theta_e} \quad (1)$$

where  $\Delta\theta_e = \lambda_0/D_l$  is the beamwidth of the element pattern. For the present example,  $N_l = 10$  for  $\text{FoV} = \pm 30^\circ$ . The number of scanned beams  $N_l$  is lower than the number of beams that are needed to scan with a single lens with diameter  $D_a$ . Therefore, a reduction of  $D_a/D_l$  in scanned beams leads to a higher lens steering performance, smaller mechanical displacement and lower lens profile. The required maximum mechanical translation of the lens array to achieve a certain FoV is given by

$$\Delta x = N_l \lambda_d f_{\#} \quad (2)$$

where  $\lambda_d$  is the wavelength in the lens medium and  $f_{\#}$  is the lens' focal length to diameter ratio. Thus, by choosing lenses with high permittivity, the required displacement is significantly smaller than those of free-standing lenses. The required translation distance is reduced by a factor of  $D_a\sqrt{\epsilon_r}/D_l = N_{RF}\sqrt{\epsilon_r}$  w.r.t a free-standing lens of the same diameter  $D_a$  and  $f_{\#}$ . The tolerance of the mechanical position  $\epsilon_{\Delta x}$  is dictated by the full array's angular beam width  $\Delta\theta_a = \lambda_0/D_a$ . This can be expressed as follows:

$$\epsilon_{\Delta x} = \frac{\Delta\theta_a}{\Delta\theta_e} \lambda_d f_{\#} = \frac{\lambda_d f_{\#}}{N_{RF}}. \quad (3)$$

The effect of the tolerance of the mechanical position  $\epsilon_{\Delta x}$  is illustrated in Fig. 2 for  $N_{RF} = 5$ . Fig. 2(a) shows the element pattern for broadside scanning ( $\theta_s = 0^\circ$ ) and a black line for a lens displaced by  $\epsilon_{\Delta x}$ . Fig. 2(b) shows the result array pattern for both cases. Note that the displaced lens element pattern will still result in a main beam pointing at broadside, but with a slightly lower directivity, in this case it is reduced by around 0.4 dB. Note that  $N_{RF}$  will impact the directivity loss due to  $\epsilon_{\Delta x}$ ; the larger  $N_{RF}$ , the smaller the loss in directivity. Moreover, as shown in Fig. 2(b), the side lobes are strongly impacted by the shift, increasing from  $-20$  to  $-12$  dB.

For submillimeter wavelength applications, the maximum translation  $\Delta x$  can be in the order of few millimeters and therefore, it is possible to implement it with piezoactuated motors

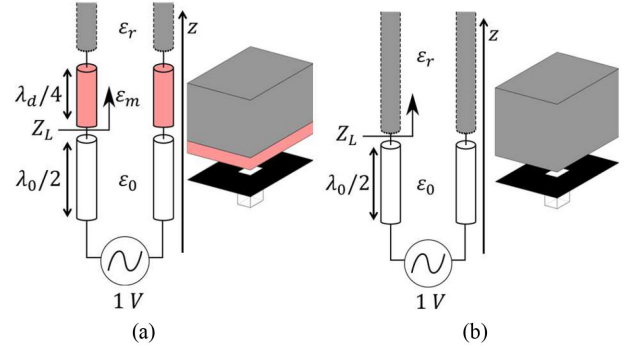


Fig. 3. Stratification and equivalent transmission line model of (a) the proposed LW antenna in this work and (b) the standard LW antenna in [31].

[26], which achieve displacements with nanometer precision, much smaller than  $\epsilon_{\Delta x}$ .

The beam steering capabilities of the phased lens array will be determined by the beam shape of the element lens pattern while scanning. In particular, the lenses should be illuminated with high aperture efficiency over the whole scanning range. To limit the spillover loss inside the lens while being translated, we impose that  $|\Delta x| \leq D_l/4$ . From (1) and (2), the field of view becomes

$$\text{FoV} \leq \frac{\sqrt{\epsilon_r}}{4f_{\#}} \quad (4)$$

where  $\epsilon_r$  is the relative permittivity of the lens which in this case is silicon,  $\epsilon_r = 11.9$ . Then, in order to achieve a  $\text{FoV} = 25^\circ$ , we need a lens  $f_{\#} \leq 1.8$ .

In the following section, a LW lens feed is designed to achieve both the goals stated above: high illumination efficiency of the lens aperture to reduce the level of the grating lobes and  $f_{\#} \approx 1.8$  inside the lens to minimize the spill over losses in the lens array element.

### III. MULTIMODE LW WAVEGUIDE FEED

In this section, we present the beam-shaping capabilities of LW feeds radiating into dense mediums when an artificially synthesized quarter-wavelength layer is added on top of a resonant air cavity. The LW feed geometry consists of a waveguide opening into a ground plane in the presence of  $\lambda_0/2$  air cavity and a dielectric transformer slab of thickness  $\lambda_0/(4\sqrt{\epsilon_m})$ , as shown in Fig. 3(a). The relative permittivity  $\epsilon_m$  is used to tune the propagation properties of LWs present in the cavity. In the following section, we analyze the LW modes and compare them to the ones in the standard stratification shown in Fig. 3(b) [31], which lacks the transformer layer. We have found that the inclusion of the quarter-wavelength transformer enables high lens aperture efficiency by exciting multiple LW modes. The use of multiple modes to illuminate quasi-optical systems was first demonstrated in [28] over a 10% bandwidth. Here, the achieved bandwidth is higher than 35%. Moreover, no double-slot iris is needed to match the input impedance of the structure to a waveguide.

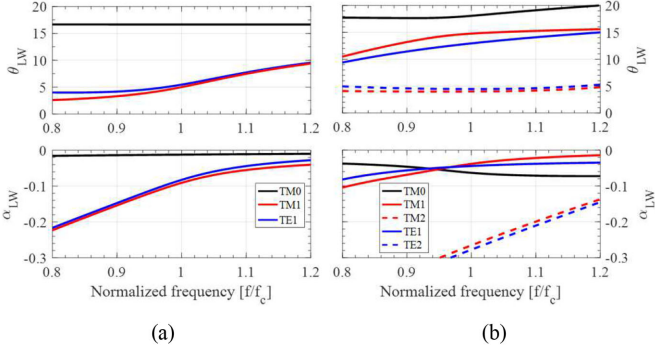


Fig. 4. Frequency dispersion diagram of the LW modes, radiating into an infinite silicon medium, in the presence of a  $\lambda_0/2$  air cavity (a) without and (b) with a  $\epsilon_m = 2.5$ -transformer.

### A. LW Mode Analysis

In the standard stratification with a half wavelength cavity below a semi-infinite dense medium [see Fig. 3(b)], there is a pair of nearly degenerate  $TM_1/TE_1$  LW mode that radiate close to broadside, plus a  $TM_0$  mode radiating toward the critical angle [31]. This  $TM_0$  mode is usually suppressed with a double slot iris in order to efficiently illuminate a lens [31]. In Fig. 4(a), the propagation constants  $k_\rho = k_0 \sqrt{\epsilon_r}(\sin \theta_{LW} - j\alpha_{LW})$ , with LW pointing angle  $\theta_{LW}$  and attenuation  $\alpha_{LW}$ , of the three modes in a silicon infinite medium are shown as a function of frequency. The  $TM_1/TE_1$  pair points toward  $\theta_{LW} \approx 5^\circ$  and a frequency-independent  $TM_0$  mode points toward  $\theta_{LW} \approx 18^\circ$ . When the transformer layer is introduced, the propagation properties of these modes as well as the number of modes change. For instance, Fig. 4(b) shows the propagation constants of the LW modes as a function of frequency when  $\epsilon_m = 2.5$ . It can be observed that there are three TM modes and two TE modes for this geometry.

To understand the topology of the different LW modes present in the stratification, it is useful to evaluate the  $\rho$ -component of the modal field inside the stratification as follows [33]:

$$e_\rho(\vec{r}) = \frac{-jk_{\rho i} \cos \phi}{2} \text{Res}(V_{TM}(k_{\rho i}, z)) H_0^{(2)}(k_{\rho i} \rho) \quad (5)$$

where  $\text{Res}(V_{TM}(k_{\rho i}, z))$  is the residue of the TM voltage solution of the transmission line in Fig. 3 evaluated at pole location  $k_{\rho i}$  (see Fig. 4), and  $H_0^{(2)}$  is the zeroth-order Hankel function of the second kind. The modal fields  $e_\rho$  corresponding to the TM modes in the standard stratification are shown in Fig. 5(a) as a function of  $z$ . The profile of the modes inside the cavity is similar to the modes that propagate in a parallel-plate waveguide (PPW) with a plate separation of  $h_0 = \lambda/2$  [32]. For instance, the  $TM_1/TE_1$  modal field resembles a  $\sin(\frac{\pi z}{h_0})$ -like shape.

When the transformer has a relative permittivity  $\epsilon_m > 5$  and thickness  $\lambda/4\sqrt{\epsilon_m}$ , the poles and resulting modal fields are very similar to the results from [31]. The presence of the quarter-wave transformer makes  $Z_L$  larger than the impedance of the infinite medium, which is the opposite effect to a standard LW radiating into free-space [34]. The LW angle and attenuation constant are larger because the impedance contrast between  $Z_L$  and  $Z_0$  is

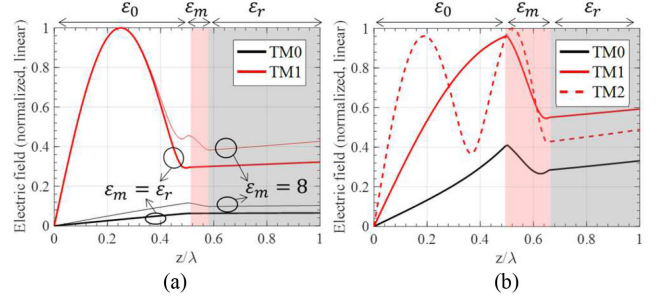


Fig. 5. TM modal fields ( $\rho$ -component) at the central frequency along  $z$  in the stratifications of (a) Fig. 3(a) with  $\epsilon_m = 8$  (thin lines) and of Fig. 3(b) (thick lines) and of (b) Fig. 3(a) with  $\epsilon_m = 2.5$ .

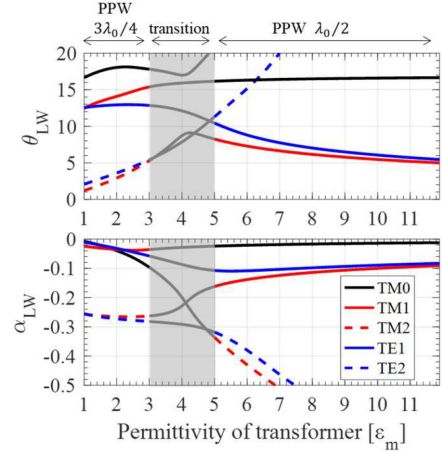


Fig. 6. LW poles present in the stratification of Fig. 3(a) at the central frequency for different choices of dielectric permittivities of the transformer layer,  $\epsilon_m$  between 1 and 11.9.

reduced. For example, the modal fields are shown in Fig. 5(a) (thin lines) for  $\epsilon_m = 8$ . The associated propagation constant at the resonant frequency is shown in Fig. 6.

When the relative permittivity of the transformer layer is small  $1 < \epsilon_m < 3$ , the reflection at the top of the cavity is very small and therefore the structure is comparable to a PPW with a plate separation of  $3\lambda_0/4$ . However, in contrast to the PPW, the  $TM_2/TE_2$  modes are not in cutoff because there is no PEC boundary condition at  $z = 3\lambda/4$ . Therefore, five modes propagate in this configuration. The frequency behavior of the five poles is shown in Fig. 4(b) for  $\epsilon_m = 2.5$ . The  $TM_0$  mode is similar to the  $TM_0$  mode in Fig. 4(a). The attenuation  $\alpha_{LW}^1$  of  $TM_1/TE_1$  poles is lower and their pointing angle  $\theta_{LW}^1 \approx 15^\circ$  is larger than without transformer. The  $TM_2/TE_2$  modes attenuate quickly and have a pointing angle  $\theta_{LW}^2 \approx 5^\circ$ . The modal field components  $e_\rho$  along  $z$  corresponding to this stratification are shown in Fig. 5(b). The  $TM_0$  and  $TM_1$  field profiles are similar to the fields shown in Fig. 5(a). It is clear that the  $TM_2$  mode shows a  $\sin(\frac{2\pi z}{h_0+h_1})$ -shape, which is similar to the profile of the  $TM_2$  mode in a PPW.

A complete overview of the five LW modes that propagate in the stratification at  $f_c$  is shown in Fig. 6 as a function of  $\epsilon_m$ . The regions  $\epsilon_m < 3$  and  $\epsilon_m > 5$  in which the LW modes

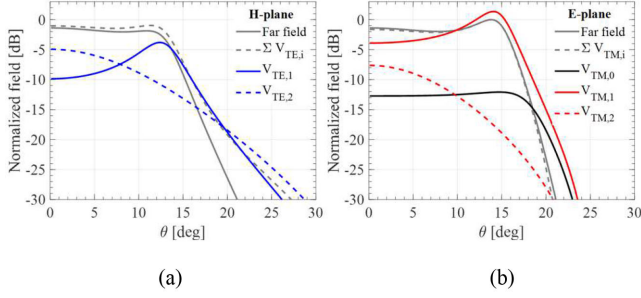


Fig. 7. Far-field radiation pattern in (a) the H-plane and (b) E-plane decomposed into the contributions from each LW pole (see Fig. 4), calculated using (6) for the stratification in Fig. 3(a) with  $\varepsilon_m = 2.5$  at the central frequency. The structure is fed by a square waveguide of size  $0.68\lambda$ .

resemble PPW modes are indicated in the figure with  $h_0 = 3\lambda/4$  and  $h_0 = \lambda/2$ , respectively. In the region  $3 \leq \varepsilon_m \leq 5$ , the TM poles switch roles which corresponds to the region, where  $Z_L \sim 120\pi$ . For example, the  $TM_0$  pole for  $\varepsilon_m < 3$  is associated with the  $TM_2$  mode for  $\varepsilon_m > 5$ . Therefore, a transition region  $3 \leq \varepsilon_m \leq 5$  is required so that the numbering of the modes and the associated field profile are consistent with both those in a PPW [32] and the stratification without transformer [31].

The far field radiated into the semi-infinite dielectric is evaluated using the spectral Green's function (SGF) approach [28]. To identify the contribution of each of these modes in the far field, the total voltage solution in the transmission line of Fig. 3(a) can be approximated around each LW pole  $k_{\rho i}$  as follows [28], [34]:

$$V_{TM/TE}(k_\rho) |_{k_\rho \approx k_{\rho i}} = \frac{2k_{\rho i}}{k_\rho^2 - k_{\rho i}^2} \text{Res}(V_{TM/TE}(k_{\rho i})). \quad (6)$$

Fig. 7 shows the far-field contribution due to each LW pole, using (6), for  $\varepsilon_m = 2.5$  and a square waveguide of size  $0.68\lambda$  (the colors correspond to the poles in Fig. 4). In the H-plane [see Fig. 7(a)], the contributions are due to TE modes, whereas the E-plane contributions [see Fig. 7(b)] are due to TM modes. The sum of the LW pole contributions (dashed gray) is a good approximation of the far field radiation pattern calculated with the nonapproximated voltage solution (solid gray). The radiation pattern resembles a “top-hat” pattern: it is nearly uniform in the region  $\theta \leq 15^\circ$  and then rapidly decays. This beam shape can be attributed to the presence of multiple LW modes that together illuminate the region nearly uniformly and results in a high aperture efficiency when it is coupled to a lens with  $f_\# = 1.8$ .

### B. Optimal Transformer Permittivity

The optimal transformer permittivity was found by evaluating the aperture efficiency of a silicon elliptical lens fed by a number of different stratifications with  $1 < \varepsilon_m < 11.9$ . Note that  $f_\#$  of the lens is different for each  $\varepsilon_m$ .

The aperture efficiency of the lens antenna was calculated in reception using a Fourier Optics (FO) approach [35] and assuming a lens with a quarter-wavelength of perfect antireflective coating at  $f_c = 550$  GHz. The optimization consisted of finding out the optimal phase center, lens  $f_\#$  and iris geometry similar to

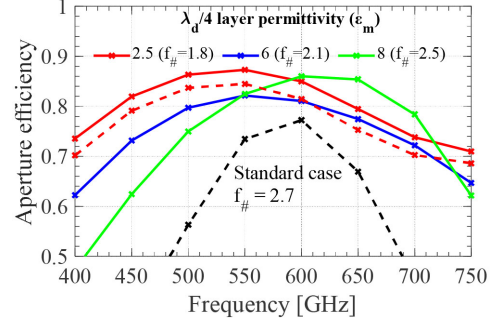


Fig. 8. Lens aperture efficiency as a function of frequency when fed by the multimode LW feed in Fig. 3(a) for different values of  $\varepsilon_m$ .  $f_\#$  of the lens varies for each permittivity. A double-slot iris has been used for the results shown in solid lines, while the red dashed line has been simulated with an open-ended square waveguide of  $0.68\lambda$ .

what it was done in [36]. With this approach, we have calculated the aperture efficiency in the frequency range 400–750 GHz of different transformer relative permittivities  $\varepsilon_m$  to determine its optimal value.

The results of the aperture efficiency optimization are shown, for several values of  $\varepsilon_m$ , in Fig. 8. The aperture efficiency bandwidth, defined as the bandwidth in which the aperture efficiency is larger than 80%, is larger for any choice of transformer permittivity than for the standard case. Furthermore, a lower transformer permittivity corresponds to a lower lens  $f_\#$ , which is consistent with the pointing angles of the main modes in Fig. 6. The optimal value for the transformer relative permittivity is found to be  $\varepsilon_m = 2.5$ , which couples to a  $f_\# = 1.8$  lens with an aperture efficiency bandwidth of 35%.

It was found that when  $\varepsilon_m > 5$ , it is necessary to suppress the  $TM_0$  mode since only the  $TE_1/TM_1$  modes will be exploited for the pattern shaping, for example, by using a double-slot iris [31]. When  $\varepsilon_m \leq 5$ , all the modes are used to synthesize the top-hat pattern as in Fig. 7 and the structure can be fed directly by an open-ended square waveguide. Specifically, using an open waveguide of size  $0.68\lambda_0$  leads to a decrease of only 2% in aperture efficiency, as shown in Fig. 8, while significantly simplifying the fabrication.

The optimized LW lens antenna has a truncation angle of  $15.5^\circ$  and a phase center of 1.44 mm below the ground plane. An overview of the single lens geometrical parameters is given in Fig. 9(a). The far-field radiation patterns (i.e., the primary patterns) into the silicon lens are shown in Fig. 9(b).

The input impedance of the waveguide in the presence of the proposed stratification has been calculated as in [28] using

$$\begin{aligned} 1/Z_{\text{in}} &= \frac{1}{4\pi^2} \iint_{-\infty}^{\infty} |M_x(k_x, k_y)|^2 G_{xx}^{hm}(k_x, k_y, z \\ &= 0) dk_x dk_y \end{aligned} \quad (7)$$

where  $G_{xx}^{hm}$  is the SGF of the structure in Fig. 3(b) and  $M_x$  is the spectral current associated with the  $TE_{10}$  waveguide mode. This result is validated with the impedance obtained from CST in

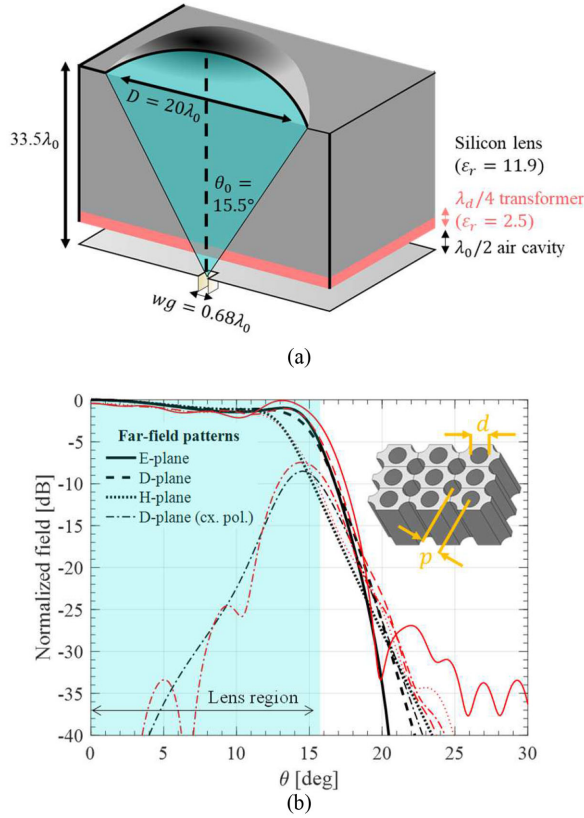


Fig. 9. (a) Cross section of a single elliptical lens array element fed with the optimized LW feed and its geometrical parameters. (b) Far-field radiation patterns into an infinite silicon medium by the lens feed shown in (a). Fields calculated using the SGF in black, full-wave results in red are done with the perforated silicon layer shown in the inset, where periodicity  $p = 79 \mu\text{m}$  and hole diameter  $d = 73 \mu\text{m}$ .

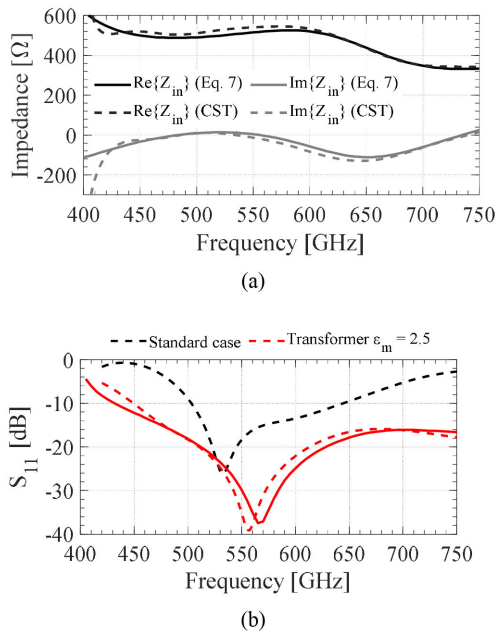


Fig. 10. (a) Waveguide impedance compared to [see Fig. 3(a)]. (b) Reflection coefficient of the optimized lens antenna with transformer layer compared to [31].

Fig. 10(a). The agreement between the result of (7) and the full-wave simulation is excellent. Furthermore,  $Z_{in}$  is not strongly frequency dependent and can be matched without a double-slot iris.

The simulated reflection coefficient is shown in Fig. 10(b), calculated using (7) and compared to the full-wave approach. The reflection coefficient is below  $-10$  dB for frequencies higher than 450 GHz. The impedance bandwidth is significantly larger than the standard structure without a transformer layer fed by a double-slot iris [31]. The bandwidth of the antenna is not limited by the impedance matching bandwidth but by the frequency dispersion of the radiation patterns.

#### IV. LENS-PHASED ARRAY PERFORMANCES

In this section, we investigate the performance of the scanning lens-phased array based on the proposed multimode LW feed. The considered array topology is the same as discussed in Section II, consisting of 19 lenses of diameter  $D_l = 20\lambda_0$  in a hexagonal grid. Each lens is fed by the waveguide-fed LW stratification discussed in Section III and is covered by a quarter-wavelength AR coating. The waveguide's E-plane is parallel to  $\hat{x}$ , according to the reference system shown in the inset of Fig. 1. The lens and array geometry are shown in Figs. 9(a) and the inset of 1, respectively.

##### A. Single Lens Element Performance

The broadside and steering properties of a single lens element at 550 GHz have been analyzed using the FO approach described in [35]. In this model, the effect of multiple reflections at the lens surface or spillover at the lens edge is not taken into account; instead, they are included as a loss in the gain. However, because of the AR coating of the lens, multiple reflections are low, and due to the proposed multimode LW feed, the spillover is low as well.

The broadside patterns radiated by a single lens element with the proposed LW feed (i.e., the secondary patterns) are shown in Fig. 11(a) and 11(b). The pattern displays good symmetry at broadside. The side-lobes are slightly lower in the H-plane due to the taper of the primary pattern in this plane [see Fig. 9(b)]. Furthermore, the pattern strongly resembles an airy pattern radiated by a  $20\lambda_0$  uniform circular current distribution (shown in red). A directivity of 35.7 dBi in the array element pattern is achieved with an aperture efficiency of 85%.

Next, the lens is displaced 2 mm relative to the feed along the E-plane. This results in a scan angle in the secondary pattern of  $19.2^\circ$ . The scanned secondary radiation pattern is shown in Fig. 11(c) in UV-coordinates. Fig. 11(d) shows the radiation pattern, where the beam has been rotated toward its maximum to show the three main planes. The radiation pattern in the H-plane is almost the same as the broadside pattern. In the E-plane, the side-lobes become 2 dB higher and the main beam is broadened. The directivity of the steerable array element pattern toward  $19.2^\circ$  is 34.6 dBi with an aperture efficiency of 54%. The scan loss (i.e., the gain relative to broadside) of the single lens is shown in Fig. 11(e). The lens can be scanned up to  $25^\circ$  (2.5 mm

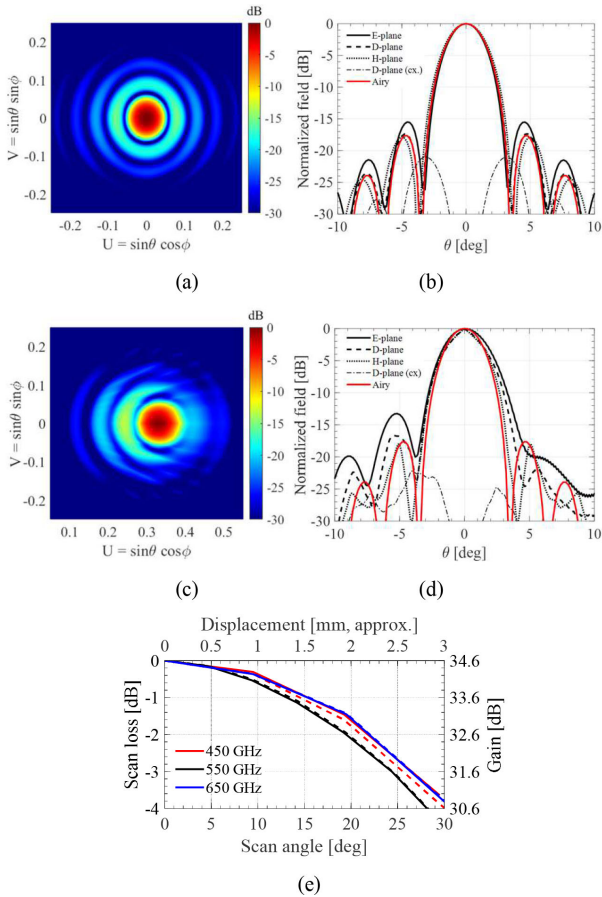


Fig. 11. Radiation pattern of a single lens for (a) and (b) broadside and (c) and (d) scanned to 20° at 550 GHz. The scan loss and gain of the lens element pattern is shown in (e) as a function of scan angle and approximate displacement.

lens displacement) in both the E- and H-planes with a loss below 3 dB. It can be seen also in the same figure that the achieved scan loss is stable over the entire 35% bandwidth.

### B. Lens-Phased Array Performance

In order to evaluate the steering properties of the 19-element lens-phased array, we multiply the obtained single lens patterns with the corresponding array factor. Since the array periodicity is very large, no mutual coupling effects will be present in this case. For broadside, all the array elements are fed in phase; for the scanned cases the lenses are fed progressively.

For broadside, Fig. 12(a) and 12(b), the grating lobe level is  $-17$  dB with a gain of 48.2 dB. When scanning to 19.2°, shown in Fig. 12(c) and 12(d), the highest grating lobe is in the E-plane and is  $-13.2$  dB. The grating lobe level is higher than the broadside case due to the lower aperture efficiency of the scanned lens, but still acceptable for many applications. The gain when scanning the array toward 19.2° is 46.7 dB. The E-plane radiation pattern is shown in Fig. 12(e) for scan angles up to 30°.

## V. LW LENS ANTENNA PROTOTYPE AT 550 GHz

A prototype at 550 GHz has been developed to validate the radiation properties of the LW feed and demonstrate the dynamic

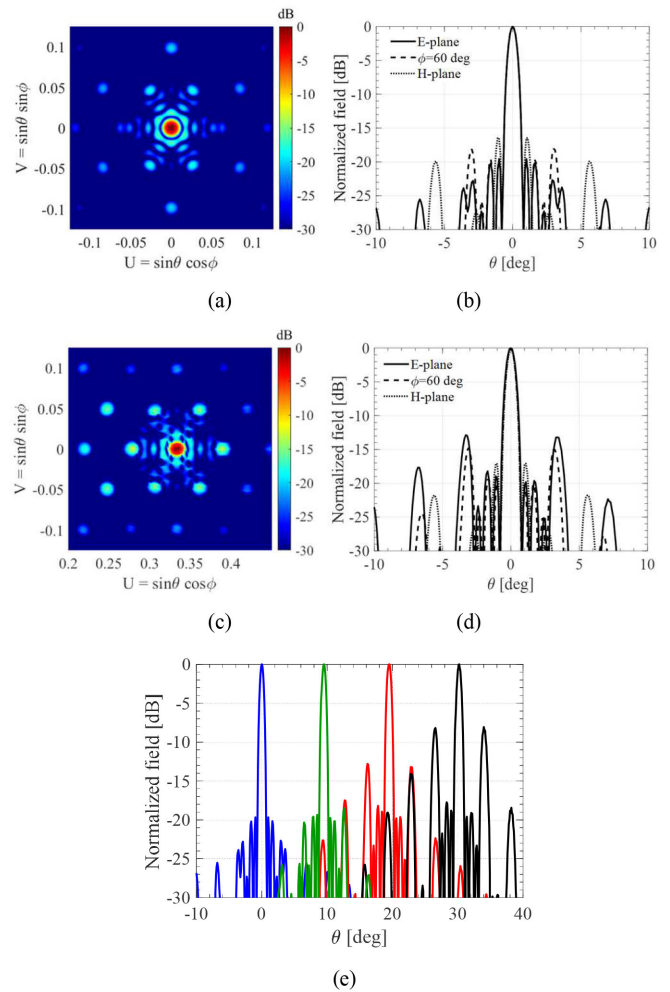


Fig. 12. Radiation pattern of a 19 lens array at 550 GHz for (a) and (b) broadside and (c) and (d) scanned to 20°. The E-plane radiation pattern is shown in (e) for scanning up to 30°.

steering capabilities of the proposed lens antenna. The prototype, shown in Fig. 13, consists of a silicon lens array where the central element is fed by the proposed LW feed. The overall array geometry is a scaled version of the one shown in Section II, in order to fit the array in the metal fixture developed in [26]. The number of elements has been reduced to 7, marked in gray in the inset of Fig. 1 and the lens diameter is around  $10\lambda_0$  instead of  $20\lambda_0$ . As a consequence of the smaller diameter, the lens surface lies in the near field of the feed. For this specific diameter of  $10\lambda_0$ , we have optimized the lens subtended angle  $\theta_0$ , as in [27], in order to achieve the maximum aperture efficiency. The resulting optimized  $\theta_0 = 17.3^\circ$  or equivalently,  $f_{\#} = 1.6$ .

The lenses, the transformer, and air cavity are synthesized in silicon wafers. This stack of wafers sits on a metal fixture, where a receiver array could be potentially integrated. In this case, the metal block consists of a straight waveguide that transforms the standard WR1.5 waveguide into a square waveguide of  $362 \times 362 \mu\text{m}$  as in [26]. The piezoelectric actuator sits on the side of this metal fixture and translates the stack of wafers in one axis. The translation displacement achieved by the prototype is

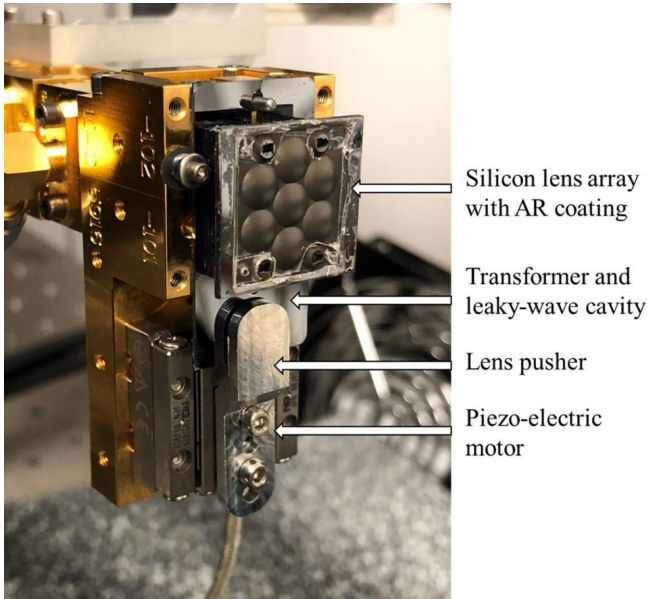


Fig. 13. Photograph of the prototype at 550 GHz that validates the embedded element pattern of the lens-phased array using an integrated piezoelectric motor to perform the mechanical scanning of the array element pattern. The height of the complete stack of wafers, including the LW cavity wafer, transformer wafer, stacked silicon wafers, and lens array wafer is 7.1 mm measured from the ground plane. The elliptical lenses subtend an angle of  $17.3^\circ$  from the focus which is 1.2 mm below the ground plane.

$\pm 1.25$  mm, i.e., a scan angle of around  $\pm 24^\circ$ , and it is executed by a piezoelectric actuator motor as in [26]. A lens pusher fixture translates the silicon stack across the LW feed using alignment metal pins as rails that support the movement of the lens.

#### A. Silicon Lens Array Wafer Stack

The silicon lens array consists of seven elliptical lenses of aperture  $D_l = 5.13$  mm ( $9.4\lambda_0$ ) and height of  $548 \mu\text{m}$  synthesized in a hexagonal configuration in order to provide a tight array spacing with high aperture efficiency. The array of lenses has been fabricated from a 1-mm high-resistivity silicon wafer using a laser micromachining and was then coated with a Parylene antireflection coating. The lens array is shown in Fig. 14.

A few other high-resistivity silicon wafers, i.e., 5 wafers of 1 mm thick and 4 wafers of  $300 \mu\text{m}$ , were stacked to create the required thickness of the array. These wafers have been processed using a DRIE process developed in [37]. The alignment of these wafers was performed using a silicon pin technique used in [38]. A silicon pin of 1 mm, shown in the inset of Fig. 14, was used in the alignment of the lens array wafer with the silicon stack. This increment in size facilitates the fabrication of the socket in the lens array with the laser without compromising the alignment. Unfortunately, the alignment of these two layers could not be measured accurately but was estimated to be better than  $20 \mu\text{m}$ .

#### B. Transformer Layer and LW Cavity

The transformer layer has been synthesized by creating an artificial dielectric from a high-resistivity silicon wafer. The

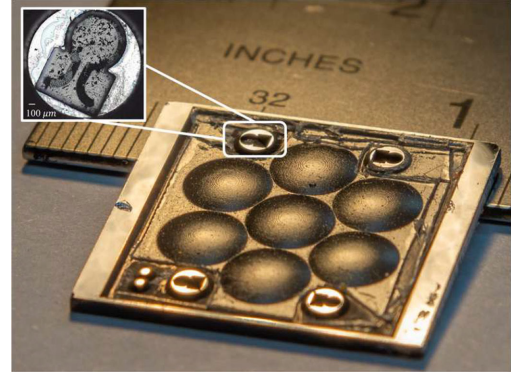


Fig. 14. Photograph of lens array wafer fabricated using laser micromachining. Inset photograph of the silicon pin alignment pin on its pocket, defining the alignment between the lens wafer and the bottom silicon wafer.

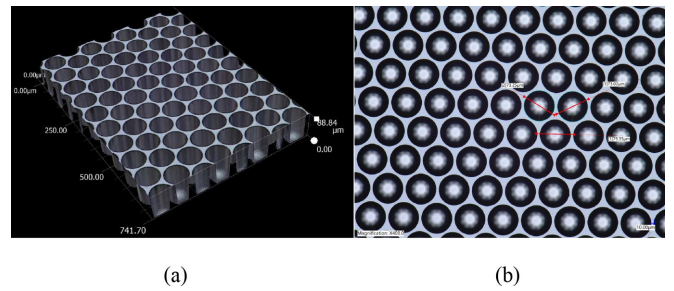


Fig. 15. (a) 3-D and (b) top view of the fabricated artificial dielectric taken under the microscope.

artificial dielectric targeted a relative permittivity of 2.5 and it was synthesized with circular perforations [39] of  $73 \mu\text{m}$  diameter to a depth of  $88 \mu\text{m}$  in a regular triangular lattice of period  $79 \mu\text{m}$ .

The validation of this artificial dielectric synthesis is shown in Fig. 9(b), where radiation patterns of the LW feed using a homogeneous dielectric layer are compared with a full-wave simulation of the perforated layer in silicon. The figure shows the good agreement between the radiation patterns and confirms the little impact that the anisotropy of synthesized dielectric has, thanks to the highly directive LW patterns. Note that the spurious radiation in the E-plane for angles larger than  $20^\circ$  is associated with the finite size of the structure in the full wave simulation.

A photograph of the perforated silicon layer and its dimensions is shown in Fig. 15. A good agreement between the fabricated and designed dimensions has been achieved using the silicon micromachining process based on DRIE [37].

The LW cavity was fabricated using a wafer of thickness  $300 \mu\text{m}$  and etching  $20 \mu\text{m}$  of the overall wafer to achieve the desired  $280 \mu\text{m}$ .

## VI. MEASUREMENTS

First, the reflection coefficient of the antenna was measured using a PNA-X and a calibrated WR-1.5 frequency extender. Its comparison with full-wave simulation is shown in Fig. 16. Note that the level of the measured reflection coefficient lies below



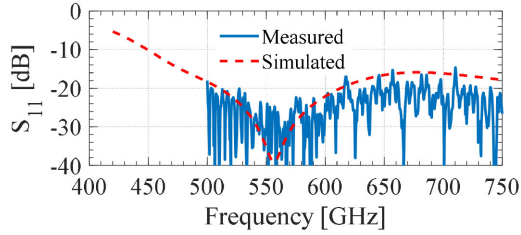


Fig. 16. Measured and simulated reflection coefficient of the embedded lens antenna array prototype measured in the WR 1.5 frequency band and plotted against full wave simulations.

the simulation due to the losses of the metal block fixture which are around 2.8 dB, as explained in [26]. But overall, the general shape of the reflection coefficient agrees well with the simulated performance of the antenna. The compression of the spring was calibrated by moving the lens back and forth with the piezo while verifying that the reflection coefficient did not have significant changes. All in all, the measured reflection coefficient is below  $-20$  dB in a bandwidth of more than 50%, which is higher than the bandwidth of the aperture efficiency for this antenna.

The embedded element pattern prototype was validated using a far-field setup similar to the one used in [26]. The prototype was connected to an *ad hoc* Schottky based transmitter that is fed by one of the synthesizers of the PNA-X to be able to fit in two rotational stages. To receive the signals, we used one of the WR1.5 PNA-X extenders as receiver and a standard gain horn. This *ad hoc* far-field setup limits the measurement band to 525 to 575 GHz, constrained by the available bandwidth of the transmitter and the scanning range was limited to  $40^\circ$  in azimuth and  $45^\circ$  in elevation.

#### A. Embedded Element Patterns

The lens array was translated with the piezoelectric motor with steps of 0.2 mm along  $\hat{y}$ , according to the reference system shown in Fig. 1. At each step, the radiation pattern of the AUT was measured. A small correction in the reference system of the radiation patterns was applied to these measurements since center of rotation of the scanner was a centimeter below the phase center of the lens array prototype. The effect of this correction is very small and it is shown in Fig. 17, where the scan angle versus displacement is compared for the corrected and the raw set of measurements. The figure also shows a good agreement between the measurements and the simulations using the aforementioned FO analysis. The solid red line shows the scan angle with the displacement for an optical system of  $f_{\#} = 1.6$  using the geometrical expression from (2). A good agreement of the measurements and simulations with this red solid line shows low  $f_{\#}$  of this multimode LW feed compared with the standard case.

Fig. 18 shows the measured radiation patterns for the central frequency at three different scan angles in the H plane, broadside,  $10^\circ$  and  $20^\circ$ , which correspond to a lens array displacement of 0, 0.5, and 1 mm. Note that the three measurements, and the rest of the scanned angles, present a small tilt of  $3.5^\circ$  in the E-plane,

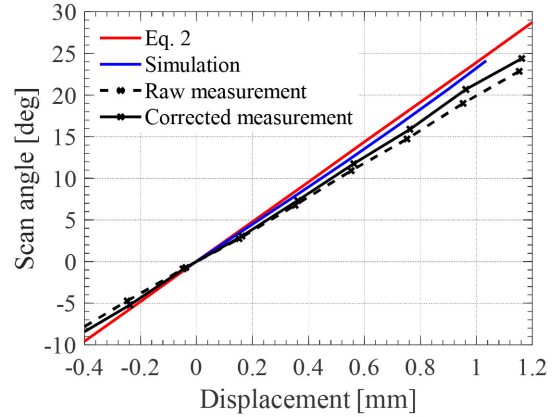


Fig. 17. Scan angle as a function of the displacement of the lens antenna array of the measured radiation patterns. The red line represents the scan angle obtained from displacing the feed of a quasi-optical system of an  $f_{\#} = 1.6$ .

that corresponds to a misalignment in  $\hat{x}$  of  $150 \mu\text{m}$  between the lens array with the feed. It is suspected that this is misalignment comes from a combination of errors and tolerances: the alignment tolerance given by the metal pins and the silicon wafer, the position accuracy between the pin pockets used in the lens wafer with respect to the actual lens array, and last, a cumulative error between the front and back alignment of the silicon pin pockets on the bulk silicon wafers employed. Nevertheless, this small tilt has barely any impact on the aperture efficiency of the antenna and it could potentially be removed with another piezoelectric motor that would allow the scanning of the array in  $\hat{x}$ . Note that this tilt has been taken into account in the simulation shown. Fig. 18 (b), (d), and (f) shows E-, H-, and D-plane cuts normalized to  $0^\circ$  of the 2-D measured radiation pattern and the FO simulations. A very good agreement between the two is shown, especially for the broadside case. The medium and large angle displacement presents slightly higher discrepancy on the side-lobe level, due to the higher spillover/reflection power presented in these cases, which is not taken into account in the FO simulation. Moreover, the relative permittivity of the quarter-wavelength Parylene antireflection coating ( $\epsilon_r = 2.62$ ) used for this lens array prototype deviates from the ideal relative permittivity ( $\epsilon_r = 3.45$ ) for a silicon lens. As presented in [26], the effects of a nonideal AR layer affect more the side-lobes while scanning. Nevertheless, the main beam and position of the nulls of the side-lobes are very close to the simulated results.

The gain loss as a function of the scan angle and relative to the broadside case is shown in Fig. 19, for the center frequency of 550 GHz and the extremes of the measured frequency band, 525 and 575 GHz. The loss is measured by taking the peak power received on each scanned position and comparing it to the gain drop evaluated using the FO simulations. Simulations and measurements differ at most 0.5 dB for the three points in the band, which we consider a very good agreement considering the limitation on the measurement setup, power fluctuations, and the effect of the multiple reflections in the lens array.

Unfortunately, the absolute gain could not be measured across the frequency due to a power fluctuation between the calibration

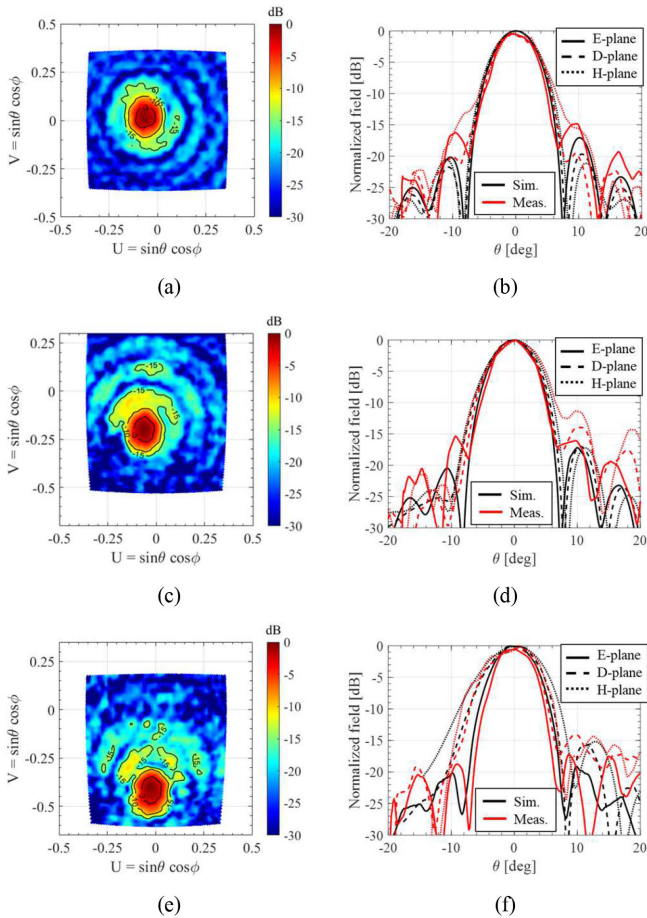


Fig. 18. Measured 2-D radiation pattern of the embedded lens antenna at 550 GHz for (a) broadside, (c)  $10^\circ$  scan angle and (e)  $19.2^\circ$  scan angle. E/H/D-Plane cuts of the measured and simulated pattern at the aforementioned scanned positions in (b), (d), (f).

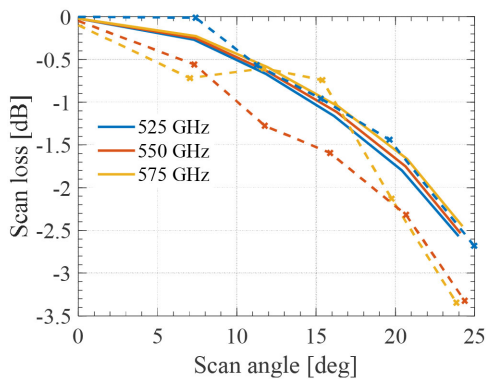


Fig. 19. Measured (dashed lines) and simulated (solid lines) gain scan loss in the H-plane normalized to the broadside case as a function of the scan angle for 525, 550, and 575 GHz.

and the actual gain measurement in this *ad hoc* measurement setup. However, considering that the fabrication techniques and materials employed for this effort are analogous to the ones presented [26], we can expect that the actual gain will be close to the simulated single lens gain of 28.2 dB.

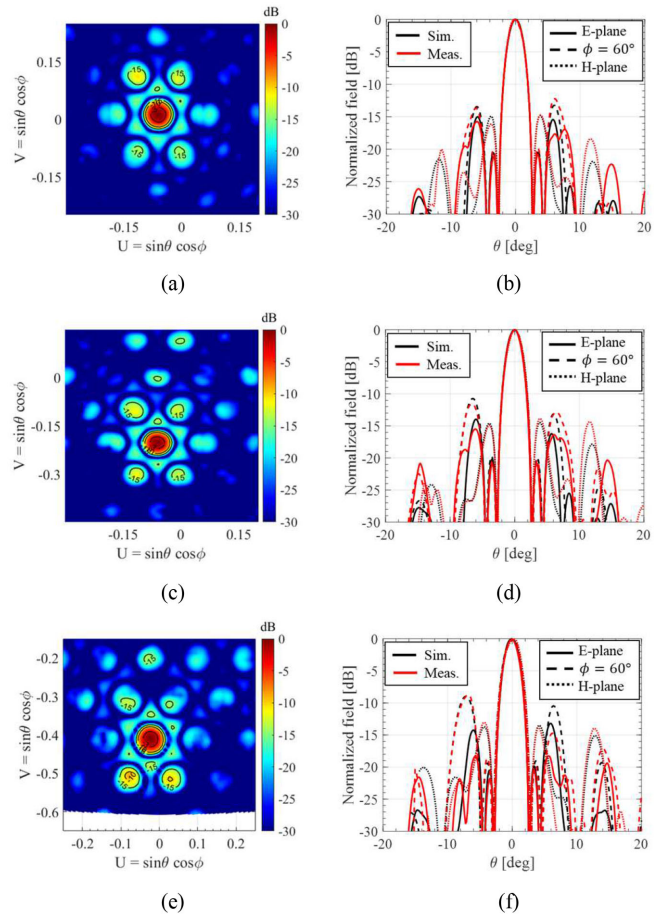


Fig. 20. Measured 2-D radiation pattern of the array at 550 GHz for (a) broadside, (c)  $10^\circ$  scan angle and (e)  $19.2^\circ$  scan angle in the H plane. E/H/D-Plane cuts of the measured and simulated pattern at the aforementioned scanned positions in (b), (d), (f).

## B. Array Patterns

In order to estimate the performance of the array, we calculated the array radiation pattern by multiplying the measured radiation patterns of the embedded lens antenna by the array factor. The array factor is composed of the seven lenses in the hexagonal pattern, as shown in gray in Fig. 1.

Fig. 20 shows the array patterns of the broadside case,  $10^\circ$  and  $20^\circ$  of scan angle. The 2-D array patterns show the multiple grating lobes from the array factor but as a result of the multiplication with the element pattern, they remain below  $-9$  dB even for the largest scan angle, in the  $60^\circ$  plane. The E-, H-, and  $60^\circ$  planes of the radiation pattern normalized to  $0^\circ$  are shown for these scan angles and plotted against the array pattern using the FO simulation. The maximum grating lobe level for broadside,  $10^\circ$  and  $19.2^\circ$  scan angle is  $-12$ ,  $-11$ , and  $-9$  dB, values that are considerably lower than other sparse arrays [12]. The results obtained with this prototype show higher grating lobes than those reported in Section IV due to the limited lens diameter, which leads to a near field illumination of the lens.

Fig. 21 shows the directivity of the array patterns for the lowest, central, and highest measured frequency, as a function

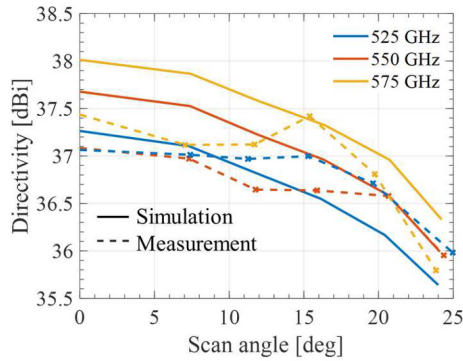


Fig. 21. Directivity as a function of the scan angle for the 7 element array for 525, 550, and 575 GHz.

of the scan angle. The simulated directivity is calculated by integrating the array pattern in the measured solid angle. The expected deviation due to this truncation is less than 0.25 dB. The agreement between the simulations and measurements is within 1 dB in the worst cases. The fluctuations in the measured directivity are due to the measurement setup, the use of a Parylene matching layer instead of an ideal one which increases the impact on the multiple reflections in the directivity, especially when scanning and the feed spill over while scanning. Note that the FO simulations of the directivity do not consider the multiple reflections inside the array.

Overall, the experimental results follow the predictions obtained from the simulations, which demonstrate the operability and performance of the new proposed LW lens feed, as well as the dynamical steering of the element pattern up to around 25° applicable in future implementations of active lens-phased arrays at these high frequencies.

## VII. CONCLUSION

A scanning lens-phased array architecture for the dynamic steering of highly directive beams at submillimeter wavelengths was presented, combining a sparse array of lenses with mechanical displacement relative to their feed. The proposed architecture drastically reduces the number of active elements compared to a fully sampled array, yet still enables wide-angle scanning.

We have derived the requirements of the lens antenna feed in order to control the level of the grating lobes over wide angles. For this purpose, we have proposed a multimode LW feed that is able to achieve an aperture efficiency greater than 80% over a bandwidth of 35% and a scan loss lower than 3 dB up to 25°. This LW feed uses a transformer layer to generate multiple modes which help to produce a top hat pattern with a suitable  $f_{\#}$  for scanning. Additionally, this layer ensures impedance matching of the feed without a double slot iris, which simplifies the fabrication process.

A prototype of an embedded lens antenna has been built at 550 GHz, integrated with a piezoelectric motor. We measured the radiation and scanning performance of the embedded pattern and combined these results with the array factor to obtain the array pattern of the phased array. We found excellent agreement between the measurement and simulated performance, validating the capability of this antenna architecture for future implementations of active lens-phased arrays.

## ACKNOWLEDGMENT

Part of this work was carried out at the Jet Propulsion Laboratory, California Institute of Technology, Pasadena, CA, USA, under a contract with the National Aeronautics and Space Administration.

## REFERENCES

- [1] C. E. Groppi and J. H. Kawamura, "Coherent detector arrays for terahertz astrophysics applications," *IEEE Trans. THz Sci. Technol.*, vol. 1, no. 1, pp. 85–96, Sep. 2011.
- [2] T. Reck *et al.*, "A silicon micromachined eight-pixel transceiver array for submillimeter-wave radar," *IEEE Trans. THz Sci. Technol.*, vol. 5, no. 2, pp. 197–206, 2015.
- [3] P. H. Siegel, "Terahertz technology in biology and medicine," *IEEE Trans. Microw. Theory Tech.*, vol. 52, no. 10, pp. 2438–2447, 2004.
- [4] D. A. Robertson *et al.*, "High resolution, wide field of view, real time 340GHz 3D imaging radar for security screening," *Proc. SPIE*, vol. 10189, May 2017, Art. no. 101890C.
- [5] S. Ochiai *et al.*, "Receiver performance of the superconducting submillimeter-wave limb-emission sounder (SMILES) on the international space station," *IEEE Trans. Geosci. Remote Sens.*, vol. 51, no. 7, pp. 3791–3802, Jul. 2013.
- [6] R. E. Cofield and P. C. Stek, "Design and field-of-view calibration of 114-660-GHz optics of the earth observing system microwave limb sounder," *IEEE Trans. Geosci. Remote Sens.*, vol. 44, no. 5, pp. 1166–1181, May 2006.
- [7] Y. Yang, O. D. Gurbuz, and G. M. Rebeiz, "An eight-element 370–410-GHz phased-array transmitter in 45-nm CMOS SOI with peak EIRP of 8–8.5 dBm," *IEEE Trans. Microw. Theory Techn.*, vol. 64, no. 12, pp. 4241–4249, Dec. 2016.
- [8] K. Guo, Y. Zhang, and P. Reynaert, "A 0.53-THz subharmonic injection-locked phased array with 63- $\mu$ W radiated power in 40-nm CMOS," *IEEE J. Solid-State Circuits*, vol. 54, no. 2, pp. 380–391, Feb. 2019.
- [9] H. Jalili and O. Momeni, "A 0.34-THz wideband wide-angle 2-D steering phased array in 0.13- $\mu$ m SiGe BiCMOS," *IEEE J. Solid-State Circuits*, vol. 54, no. 9, pp. 2449–2461, Sep. 2019.
- [10] J. V. Siles, R. Lin, P. Bruneau, C. Lee, and I. Mehdi, "An ultra-compact 16-pixel local oscillator at 1.9 THz," in *Proc. Int. Conf. Infrared, Millimeter, THz Waves, IRMMW-THz*, vol. 2016–Nov., pp. 1–2, 2016.
- [11] I. Mehdi, J. Siles, C. Lee, and R. Lin, "Compact submillimeter-wave multipixel local oscillator sources," in *Proc. 40th Int. Conf. Infrared, Millimeter, THz Waves*, 2015, pp. 1–2.
- [12] R. Mailloux, L. Zahn, and A. Martinez, "Grating lobe control in limited scan arrays," *IEEE Trans. Antennas Propag.*, vol. AP-27, no. 1, pp. 79–85, Jan. 1979.
- [13] D. Blanco, N. Llombart, and E. Rajo-Iglesias, "On the use of leaky wave phased arrays for the reduction of the grating lobe level," *IEEE Trans. Antennas Propag.*, vol. 62, no. 4, pp. 1789–1795, Apr. 2014.
- [14] F. Scattoni, M. Ettorre, R. Sauleau, and N. J. G. Fonseca, "A flat-topped leaky-wave source for phased arrays with reduced scan losses," in *Proc. 8th Eur. Conf. Antennas Propag.*, The Hague, 2014, pp. 1220–1224.
- [15] B. Avser, J. Pierro, and G. M. Rebeiz, "Random feeding networks for reducing the number of phase shifters in limited-scan arrays," *IEEE Trans. Antennas Propag.*, vol. 64, no. 11, pp. 4648–4658, Nov. 2016.

- [16] D. Petrolati, P. Angeletti, and G. Toso, "A lossless beam-forming network for linear arrays based on overlapped sub-arrays," *IEEE Trans. Antennas Propag.*, vol. 62, no. 4, pp. 1769–1778, Apr. 2014.
- [17] R. Beresford *et al.*, "Eyes on the sky: A refracting concentrator approach to the SKA." The Executive Secretary Australian SKA Consortium Committee, Epping, NSW, Australia, Jun. 2002, Art no. 1710.
- [18] J. R. James, C. M. Hall, and G. Andrasic, "Microstrip elements and arrays with spherical dielectric overlays," *Proc IEE Proc. H - Microw., Antennas Propag.*, vol. 133, no. 6, pp. 474–482, Dec. 1986.
- [19] J. C. R. Poirier, G. A. Morin, Y. M. M. Antar, and J. W. Moffat, "Millimetre-wave limited-scan array using small lenses," *IEEE Antennas Propag. Soc. Int. Symp. Dig., Held Conjunction With: USNC/URSI Nat. Radio Sci. Meeting (Cat. No.01CH37229)*, Boston, MA, USA, 2001, pp. 823–826 vol. 2.
- [20] I. V. Minin and O. V. Minnin, *Basic Principles of Fresnel Antenna Arrays*. New York, NY, USA: Springer, 2008.
- [21] M. Zimmermann, I. Timofeev, and K. E. Linehan, "Lensed antennas for use in cellular and other communications systems," Grant US-10418716-B2, 2019.
- [22] S. Matysine, L. Matysine, and A. Demarco, "Lens arrays configurations for improved signal performance," US20170040705, Sep. 02, 2017.
- [23] P. Clinton, J. Scarborough, P. Tupin, and F. DiFonzo, "Lens antenna system," US20180269576A1, Sep. 20, 2018.
- [24] G. Mumcu, M. Kacar, and J. Mendoza, "Mm-Wave beam steering antenna with reduced hardware complexity using lens antenna subarrays," *IEEE Antennas Wireless Propag. Lett.*, vol. 17, no. 9, pp. 1603–1607, Sep. 2018.
- [25] S. Bosma, M. Alonso-delPino, C. Jung-Kubiak, D. Blanco, and N. Llombart, "Scanning lens phased array for submillimeter wavelengths," in *Proc. 44th Int. Conf. Infrared, Millimeter, THz Waves*, Sep. 2019, pp. 1–2.
- [26] M. Alonso-delPino, C. Jung-Kubiak, T. Reck, N. Llombart, and G. Chattopadhyay, "Beam scanning of silicon lens antennas using integrated piezomotors at submillimeter wavelengths," *IEEE Trans. THz Sci. Technol.*, vol. 9, no. 1, pp. 47–54, Jan. 2019.
- [27] M. Alonso-DelPino *et al.*, "Design guidelines for a terahertz silicon microlens antenna," *IEEE Antennas Wireless Propag. Lett.*, vol. 12, pp. 84–87, 2013.
- [28] A. Neto, N. Llombart, G. Gerini, M. D. Bonnedal, and P. de Maagt, "EBG enhanced feeds for the improvement of the aperture efficiency of reflector antennas," *IEEE Trans. Antennas Propag.*, vol. 55, no. 8, pp. 2185–2193, Aug. 2007.
- [29] T. Reck and B. Drouin, "Submillimeter-wave spectrometer for small satellites," in *Proc. 14th Meeting Venus Exploration Anal. Group*, NASA Headquarters, Washington, DC, USA, Nov. 29–Dec. 1, 2016.
- [30] C. S. Ruf, C. T. Swift, A. B. Tanner, and D. M. Le Vine, "Inferometric synthetic aperture microwave radiometry for the remote sensing of the earth," *IEEE Trans. Geosci. Remote Sens.*, vol. 26, no. 5, pp. 597–611, Sep. 1988.
- [31] N. Llombart, G. Chattopadhyay, A. Skalare, and I. Mehdi, "Novel terahertz antenna based on a silicon lens fed by a leaky wave enhanced waveguide," *IEEE Trans. Antennas Propag.*, vol. 59, no. 6, pp. 2160–2168, Jun. 2011.
- [32] D. M. Pozar, *Microwave Engineering*. 3rd ed. Wiley, 2005.
- [33] A. Polemi and S. Maci, "On the polarization properties of a dielectric leaky wave antenna," *IEEE Antennas Wireless Propag. Lett.*, vol. 5, pp. 306–310, 2006.
- [34] D. R. Jackson and A. A. Oliner, "A leaky-wave analysis of the high-gain printed antenna configuration," *IEEE Trans. Antennas Propag.*, vol. 36, no. 7, pp. 905–910, Jul. 1988.
- [35] H. Zhang, S. O. Dabirnezare, G. Carluccio, A. Neto, and N. Llombart, "A GO/FO Tool for analyzing quasi-optical systems in reception," in *Proc. 44th Int. Conf. Infrared, Millimeter, THz Waves*, Paris, France, 2019, pp. 1–2.
- [36] M. Arias Campo, D. Blanco, S. Bruni, A. Neto, and N. Llombart, "On the use of fly's eye lenses with leaky-wave feeds for wideband communications," *IEEE Trans. Antennas Propag.*, vol. 68, no. 4, pp. 2480–2493, Apr. 2020.
- [37] C. Jung-Kubiak *et al.*, "A multistep DRIE process for complex terahertz waveguide components," *IEEE Trans. THz Sci. Technol.*, vol. 6, no. 5, pp. 690–695, Sep. 2016.
- [38] M. Alonso-delPino, T. Reck, C. Jung-Kubiak, C. Lee, and G. Chattopadhyay, "Development of silicon micromachined microlens antennas at 1.9 THz," *IEEE Trans. THz Sci. Technol.*, vol. 7, no. 2, pp. 191–198, Mar. 2017.
- [39] M. Mrnka and Z. Raida, "An effective permittivity tensor of cylindrically perforated dielectrics," *IEEE Antennas Wireless Propag. Lett.*, vol. 17, no. 1, pp. 66–69, Jan. 2018.



**Maria Alonso-delPino** (Senior Member, IEEE) received the degree in telecommunications engineering from the Technical University of Catalonia (UPC), Barcelona, Spain, in 2008; the M.S. degree in electrical engineering from the Illinois Institute of Technology, Chicago, IL, USA, in 2008; and the Ph.D. degree in signal theory and communications/electrical engineering from UPC in 2013.

From 2014 to 2015, she was a Postdoctoral Researcher with the Technical University of Delft (TU Delft), Delft, The Netherlands. From 2015 to 2016,

she was a NASA Postdoctoral Fellow with the Jet Propulsion Laboratory (JPL), Pasadena, CA, USA. From 2016 to 2020, she was a Member of the Technical Staff at the Submillimeter Wave Advanced Technology Group of JPL/NASA. Since 2020, she has been an Assistant Professor with TU Delft. Her interests include millimeter and submillimeter-wave heterodyne and direct detection technologies, antennas, quasi-optical systems.

Dr. Alonso-delPino was the recipient of the Outstanding Reviewer Award of the IEEE TRANSACTIONS ON TERAHERTZ SCIENCE AND TECHNOLOGY in 2013 and the co-recipient of the 2014 IEEE Terahertz Science and Technology Best Paper Award.



**Sjoerd Bosma** (Student Member, IEEE) received the B.Sc. and M.Sc. (*cum laude*) degrees in electrical engineering from the Delft University of Technology, Delft, The Netherlands, in 2015 and 2017, respectively. He is currently working toward the Ph.D. degree with the Terahertz Sensing Group, TU Delft, where he works on leaky-wave lens antenna arrays.

From September 2018 to February 2019, he participated in the JPL Visiting Student Researcher Program, Jet Propulsion Laboratory, CA, USA.



**Cecile Jung-Kubiak** (Senior Member, IEEE) received the master's degree in physics and materials chemistry from Polytech'Montpellier, Montpellier, France, in 2006 and the Ph.D. degree in physics from Universite Paris-Sud XI, Orsay, France, in 2009.

She was the recipient of a 2-year NASA Postdoctoral Fellowship at the California Institute of Technology in 2010, and is now a Member of the Technical Staff for the S.W.A.T. Group, Jet Propulsion Laboratory, in Pasadena, USA. Her research interests include the development of silicon micromachining technologies

using DRIE techniques, the miniaturization of multi-pixel arrays to build compact 3-D instruments and GaAs-based frequency multipliers and mixers in the THz region. She has coauthored more than 60 papers in international journals and conferences, holds several patents.

Dr. Jung-Kubiak was a recipient of the 2010 JPL Outstanding Postdoctoral Research Award in the field of Technology, Instrumentation, and Engineering and the 2014 IEEE THz Science and Technology Best Paper Award.



**Goutam Chattopadhyay** (Fellow, IEEE) received the Ph.D. degree in electrical engineering from the California Institute of Technology (Caltech), Pasadena, CA, USA, in 2000.

He is a Senior Research Scientist with the NASA's Jet Propulsion Laboratory, California Institute of Technology, and a Visiting Associate with the Division of Physics, Mathematics, and Astronomy, California Institute of Technology, Pasadena, CA, USA. He has authored or coauthored more than 350 publications in international journals and conferences and

holds more than 20 patents. His research interests include microwave, millimeter wave, and terahertz receiver systems and radars, and development of terahertz instruments for space applications.

Dr. Chattopadhyay was the recipient of more than 35 NASA technical achievement and new technology invention awards, the IEEE Region-6 Engineer of the Year Award in 2018, the Distinguished Alumni Award from the Indian Institute of Engineering Science and Technology, India, in 2017, the Best Journal Paper Award in 2020 and 2013 by the IEEE TRANSACTIONS ON TERAHERTZ SCIENCE AND TECHNOLOGY, the Best Paper Award for antenna design and applications at the European Antennas and Propagation conference in 2017, and the IETE Prof. S. N. Mitra Memorial Award in 2014. He is an elected AdCom member of the IEEE MTT Society and is the Chair of the Meetings and Symposia Committee. He is a Fellow of IETE (India) and an IEEE Distinguished Lecturer.



**Nuria Llombart Juan** (Fellow, IEEE) received the master's degree in electrical engineering and the Ph.D. degree from the Polytechnic University of Valencia, Valencia, Spain, in 2002 and 2006, respectively.

During her master's degree studies, she spent one year with the Friedrich Alexander University of Erlangen Nuremberg, Erlangen, Germany, and with the Fraunhofer Institute for Integrated Circuits, Erlangen, Germany. From 2002 to 2007, she was with the Antenna Group, TNO Defense, Security and Safety

Institute, The Hague, The Netherlands, working as a Ph.D. Student and afterward as a Researcher. From 2007 to 2010, she was a Postdoctoral Fellow with the California Institute of Technology, working with the Submillimeter Wave Advance Technology Group, Jet Propulsion Laboratory, Pasadena, CA, USA. She was a "Ramón y Cajal" Fellow in the Optics Department, Complutense University of Madrid, Madrid, Spain, from 2010 to 2012. In September 2012, she joined the THz Sensing Group, Technical University of Delft, Delft, The Netherlands, where as of February 2018 she was a Full Professor. She has coauthored more than 200 journal and international conference contributions in the areas of antennas and THz systems.

Dr. Llombart was the recipient H. A. Wheeler Award for the Best Applications Paper of 2008 in the IEEE TRANSACTIONS ON ANTENNAS AND PROPAGATION, the 2014 THz Science and Technology Best Paper Award of the IEEE Microwave Theory and Techniques Society, and several NASA awards. She was also the recipient of the 2014 IEEE Antenna and Propagation Society Lot Shafai Mid-Career Distinguished Achievement Award. She serves as a Board Member of the IRMMW-THz International Society and Associate Editor of IEEE TRANSACTIONS ON ANTENNAS AND PROPAGATION. In 2015, she was the recipient of European Research Council Starting Grant. In 2019, she became IEEE Fellow for contributions to millimeter and submillimeter wave quasi-optical antennas.